# Potassium-ion batteries using KFSI in monoglyme electrolytes: Implications of cation solvation on the K+-graphite (co-)intercalation mechanism

Phuong Nam Le Pham, Vincent Gabaudan, Athmane Boulaoued, Gustav Åvall, Patrik Johansson, Laure Monconduit, Lorenzo Stievano, Fabrice Salles

# Potassium-ion batteries using KFSI in monoglyme electrolytes: Implications of cation solvation on the $K^+$-graphite (co-)intercalation mechanism

Phuong Nam Le Pham[1,2], Vincent Gabaudan[1], Athmane Boulaoued[3], Gustav Åvall[3], Fabrice Salles[1], Patrik Johansson[2,3], Laure Monconduit[1,2,4] and Lorenzo Stievano[1,2,4]

1- ICGM, Univ. Montpellier, CNRS, Montpellier, France

2- Alistore-ERI, CNRS FR 3104, Amiens, France

3- Department of Physics, Chalmers University of Technology, Göteborg, Sweden

4- RS2E, CNRS, Amiens, France

**Abstract**

Recently potassium-ion batteries have been proposed as a promising next generation battery technology owing to cost effectiveness and a wide range of electrode materials as well as electrolytes available. Potassium bis(fluorosulfonyl)imide (KFSI) in monoglyme (DME) is one potential electrolyte, wherein the $K^+$ solvation heavily depends on the salt concentration and strongly affects the electrochemistry. Pure $K^+$ intercalation occurs for highly concentrated electrolytes (HCEs), while co-intercalation is dominant for less concentrated electrolytes. The mechanisms are easily distinguished by their galvanostatic curves as well as by *operando* XRD. Here Raman spectroscopy coupled with computational chemistry is used to provide in-depth knowledge about the cation solvation for a wide concentration range, all the way up to 5 M KFSI in DME. Starting from pure DME experimental and computed Raman spectra provides a detailed conformational assignment enabling us to calculate solvation numbers (SNs) of $K^+$ by DME as a function of salt concentration for all the electrolytes. For low to medium KFSI concentrations, the SN is approximately constant, *ca.* 2.7, and/as there is a surplus of DME solvent available, while for HCEs, with much less DME available, the SN is <2. This reduced SN results in a thermodynamically more favored desolvation at the graphite surface, leading to intercalation, as compared to the higher SN of conventional electrolytes leading to co-intercalation, as observed also by electrochemical cycling.

## 1. Introduction

The rapid increase in the global energy demand urges for a faster development of additional energy storage technologies both to meet demand and circumvent/mitigate resource and cost issues [1]. It is today clear that much of that demand will be for electrochemical storage in the shape of various batteries – their efficiencies and versatilities lead the way [2]. Being commercialized in the early 1990s, lithium-ion batteries (LIBs) reign the power source market for a wide range of applications: from portable devices to electric vehicles [3,4]. This can lead to a depletion of lithium reserve in the Earth's crust [5] and therefore next generation batteries are needed. Amongst the post-LIB technologies researched, potassium-ion batteries (KIBs) have recently attracted huge interest owing to the high availability of potassium and foreseen comparable cell energy densities to both LIBs and some post-LIBs, such as sodium-ion batteries (SIBs) [6,7]. Moreover, potassium forms no alloys with aluminum, and hence there is, as for SIBs but in contrast to LIBs, no need for expensive copper current collectors.

Graphene-based materials recently attracted a huge attention due to their applicability in energy storage [8–11]. Amongst those, graphite – the well-known negative electrode material in commercial LIBs – has significant promise also for KIBs due to its ability to intercalate $K^+$ ions, with a resulting high reversible specific capacity of 278 mAh/g, corresponding to the formation of $KC_8$ [12–17]. However, its electrochemical behavior strongly depends on the electrolyte; a conventional $KPF_6$ in EC/DEC electrolyte has relatively low compatibility, towards both graphite and K metal, and results in substantial capacity losses and relatively short cycle-life of cells [12,18]. In contrast, glyme-based electrolytes, in particular those based on 1,2-dimethoxyethane (a k a monoglyme, G1 or DME), such as the herein used potassium bis(fluorosulfonyl)imide (KFSI) in DME electrolytes, have a high compatibility to both graphite [19,20] and K metal [21,22]. The electrolyte salt concentration, however, can alter the storage mechanism, and hence the capacity, as proven by graphite half-cell experiments to vary from $K(DME)_x$ co-intercalation to $K^+$ intercalation [19,23–25]. Both mechanisms, co-intercalation and intercalation, have already been thoroughly discussed in many reviews of LIBs and SIBs [26–32] and are commonly related to the presence of a stable solid electrolyte interphase (SEI) acting as a solvent-blocking layer [33–36]. The co-intercalation of $Na^+$ with diglyme in graphite occurs reversibly with excellent rate and cycling performance [37], either due to negligible SEI formed, both for graphite [38] and hard carbon [39], and/or a specific stabilization of the $Na^+$-diglyme complex (within graphite) [40]. Some recent reports on the stability of the SEI formed by DME-based electrolytes in KIBs show improved coulombic efficiency and cycling retention of graphite [41,42], but its influence on the charge storage mechanism has not been clarified yet.

As an alternative and/or additional factor, the cation solvation has been suggested to affect the storage mechanism [43,44], as this is a function of the electrolyte salt concentration. At low salt concentrations each cation has a relatively stable first solvation shell, often predominantly composed of solvent, since weakly coordinating anions such as the FSI anion are often employed, and comparatively high solvation number (SN) and coordination number (CN). With increasing salt concentration, the SN at some point starts to decrease and this is often concurrent with anions replacing solvent, leading to contact ion-pairs (CIPs) and higher aggregates (AGGs). We expected the same for KFSI in DME, but while many efforts have been made to understand the solvation of $K^+$-DME systems by Raman spectroscopy [21,45,46], yet none of them have provided an unambiguous picture. This is much due the conformational flexibility of pure DME, existing as five stable conformers: TGG, TGG', TGT, TTG and TTT at 20 °C [47] (see SI section for more details),

that each have different cation coordinating properties. To resolve this, density functional theory (DFT) calculations together with Raman spectroscopy can provide thermodynamic properties, *i.e.* relative stabilities of both conformers and complexes, as well as Raman activities for each, and experimental verification with high accuracy.

Herein, we investigate the $K^+$ cation solvation for various differently concentrated KFSI in DME electrolytes by a combined Raman spectroscopy and DFT approach, and correlate this bulk local electrolyte structure to the observed storage mechanism in graphite obtained by *operando* X-ray diffraction (XRD). To further clarify the intercalation mechanism Monte Carlo (MC) simulations were performed to provide additional information on the DME to $K^+$ ratio and organization in the interlayer spacing of graphite.

## 2. Experimental and computational methods

### 2.1. *Sample preparation*

KFSI (99.90%, Solvionic) and DME (99.50%, Sigma-Aldrich) were used as received. A series of KFSI in DME electrolytes was prepared by simple mixing of stoichiometric amounts using magnetic stirring, with solvent-to-salt molar ratios from 1.5 to 30, *i.e. ca.* 0.5 – 6 M, inside an argon-filled glove box ($H_2O$ <5 ppm, $O_2$ ≤1 ppm). Pure DME and all electrolytes were stored in sealed glass vials before any measurements.

### 2.2. *Electrode preparation and electrochemical tests*

Graphite (SLP6, TIMCAL$^{TM}$) was mixed with carboxymethyl cellulose, CMC, as the binder with the mass ratio of 90:10 in deionized water using planetary ball milling. The slurry was then coated on copper foil (17.5 μm, Goodfellow) using the doctor blade method. The film was dried under vacuum at 80 °C for 12 h and then cut into 12.7 mm diameter electrodes (area = 1.27 $cm^2$).

CR2032 stainless steel coin cells were assembled in an argon-filled glove box using a graphite electrode, a potassium metal disk (Sigma-Aldrich, 99.5%) as the counter-electrode, and a Whatman glass fibre separator. Three electrolytes, with DME:KFSI molar ratios of 15:1, 3:1 and 2:1, respectively, corresponding to *ca.* 1.0, 3.0 and 5.0 M, were selected for the electrochemical tests wherein the galvanostatic profiles were recorded at a current density of 25 mA/g in the voltage range 0–2 V *vs.* $K^+/K°$ using an MPG-2 (Biologic) potentiostat. In order to evaluate the role of the SEI, two special experiments were carried out by cycling graphite | K half-cells using 1.0 and 5.0 M electrolytes one single cycle, after which the SEIs are well-formed. Subsequently, the cells where cycled with "the other" electrolyte at the same current density.

### 2.3. Operando *X-ray diffraction (XRD)*

*Operando* XRD was carried out using a special *in situ* electrochemical cell [48] equipped with a beryllium window as one of the current collectors onto which graphite powder was put. These experiments used a current density of 10 mA/g and diffraction patterns were collected on an Empyrean diffractometer (PANalytical) using Co Kα radiation in the 2θ range 15–43° for an acquisition time of 1 h.

### 2.4. *Raman spectroscopy*

The Raman spectroscopy was carried out using a Bruker MultiRam FT-Raman spectrometer with a 1064 nm excitation line (Nd:YAG) at a laser power of 250 mW. Raman spectra were recorded between 200 and 1700 $cm^{-1}$ at a resolution of 2 $cm^{-1}$ and averaged over 2000 scans. For the more

detailed analyses, the spectral region 680–1045 $cm^{-1}$ was fitted to several Voigt profiles and deconvoluted using PeakFit™. The $R^2$ was 0.997 for pure DME and 0.999 for all other cases.

### 2.5. *Computational chemistry*

Optimized configurations for the five conformations of DME (TGG, TGG', TGT, TTG and TTT) and their complexes with $K^+$, $[K(DME)_x]^+$ (x = 1-5, depending on the conformer), were all obtained from DFT calculations using the Gaussian 16 software [49] at the M06-2X/6-311++G(d,p) level of theory [50]. A polarizable continuum model (PCM) [51] using the dielectric constant of DME ($\varepsilon = 7.2$) was employed to implicitly account for solvation effects. The relative energies and entropies ($E_r$) were calculated using TGT as reference. The populations of DME conformers were considered to follow a Boltzmann distribution (Table S1). The binding energies ($\Delta E_{bind}$) for the $[K(DME)_x]^+$ complexes were calculated as:

$$\Delta E_{bind} = E_{K(DME)_x^+} - (E_{K^+} + xE_{DME}) \quad (1)$$

The vibrational frequencies and Raman activities were subsequently computed analytically for the converged geometries as 2nd and 3rd derivatives of the energies, respectively. The vibrational modes were assigned manually using visualization in the Avogadro software [52]. Artificial Raman spectra for both pure DME and a few electrolytes were constructed using GaussSum [53] using a frequency scaling factor of 0.953 [54]and a FWHM of 16 $cm^{-1}$.

Complementary to the DFT calculations, classical MC simulations were performed to investigate the plausible organization of DME and $K^+$ cations in the interlayer spacing of graphite ($KC_x$). Geometry optimizations were performed for DME in TGT conformation using DFT and the GGA/PBE functional and partial charges were determined using the Mulliken scheme in $DMol^3$, while the electronegativity equalization method (qEq as implemented in Materials Studio) was used for $K(DME)_xC_y$. For $[K(DME)_x]$ the charge was fixed to 1. For the MC simulations, the Universal Force Field (UFF) was used to reproduce the Lennard Jones (LJ) interactions [55] and NVT calculations [56], with a fixed number of cations (required to have a neutral system as a function of the $KC_x$ composition) and molecules (corresponding to the saturation of the interlayer spacing), were performed at 300 K, with 5 million steps for equilibration and 2 million steps for production. The electrostatic interactions were calculated by Ewald summation [56], while the short-range contributions corresponding to LJ parameters were computed using the Lorentz-Berthelot rules. Simulations were conducted using multi-cells, 6x3x1 unit cells, consistent with a cut-off distance for LJ interactions at 12 Å, and built with the experimentally determined interlayer spacing.

## 3. Results and discussion

The evolution of the storage mechanism as a function of the electrolyte salt concentration and of both galvanostatic and *operando* XRD profiles is introduced first, followed by the investigation of the solvation of $K^+$ in DME by the combined DFT-Raman spectroscopy approach. Finally, these findings are used to gain insight into the possible influence of cation solvation in the storage mechanism of potassium in graphite.

### 3.1. *Intercalation mechanism*

The galvanostatic profiles and the evolution of the capacity with cycling of K/graphite half-cells using electrolytes with different concentrations are shown in Figure 1. The electrochemical profile of the half-cell containing the least concentrated electrolyte, 1.0 M, is typical of co-intercalation, with a high-potential pseudo-plateau at 0.8 V and a relatively low reversible capacity (92 mAh/g). These results thoroughly agree with previous works on the potassiation of graphite using a $KPF_6$ in DME

electrolyte[18,23]. During the second discharge, irreversible phenomenon occurs between 0.1 and 0 V, which rapidly leads to the complete inactivation of the battery after only a few cycles. The origin of this phenomenon, not observed during the first discharge, is not yet completely understood. Indeed, in the case of Na//graphite systems utilizing the co-intercalation mechanism, such a behavior was attributed to the decomposition of FSI, where significant CO and $C_2H_4$ gas evolution was observed at low potentials, and $H_2$ gas evolution in symmetric sodium cells, showing that the salt is unstable towards both graphite during co-intercalation reactions and sodium metal [57]. Previous works using $KPF_6$-based glyme electrolytes did not produce such a low voltage plateau during potassium co-intercalation in graphite [23], indicating that the salt is crucial for the stability of these systems. Nonetheless, the possible degradation path of FSI is unclear, and might involve possible redox shuttle species that are formed only after a full potassiation/depotassiation cycle. Moreover, one cannot exclude that such a low potential process represents potassium plating on the surface of graphite caused by the capture of solvated cation in the growing SEI layer [58], a common issue reported for LIBs [59,60]. Nevertheless, the lack of the typical pattern of K metal in the *operando* XRD data does not support the formation of such phase along the low potential plateau.

When using the 5.0 M electrolyte, only two low-potential plateaus are observed, with a corresponding reversible capacity of *ca.* 280 mAh/g. Here, the charge/discharge curves for the first and the second cycles are similar to those obtained for the simple intercalation of $K^+$ in graphite using carbonate-based electrolytes [13,61,62].

The most puzzling charge/discharge profile, however, is that of the 3.0 M electrolyte: a reduced high-potential pseudo-plateau is followed by two additional plateaus at 0.25 and 0.15 V. Interestingly, the shape of the curve is similar to the sequential combination of the processes observed for the 1.0 and 5.0 M electrolytes. The first plateaus contribute with *ca.* 40 mAh/g to the total capacity of the first discharge, while at the end of the low potential plateau a total capacity of *ca.* 300 mAh/g is observed.

Such a large capacity exceeds the theoretical one for graphite corresponding to the formation of $KC_8$, the excess capacity being possibly due to sluggish mass transport of the inserted species exiting the host and irreversible capacity loss caused by the decomposition of the electrolyte. Indeed, a more reasonable reversible capacity of 250 mAh/g is recovered during the following charge,

The evolution of the capacity upon cycling (Figure 1b) is very bad for the cell with the least concentrated electrolyte, whereas an excellent reversibility was observed for the other cells, with a Coulombic efficiency approaching 100% after a few cycles.

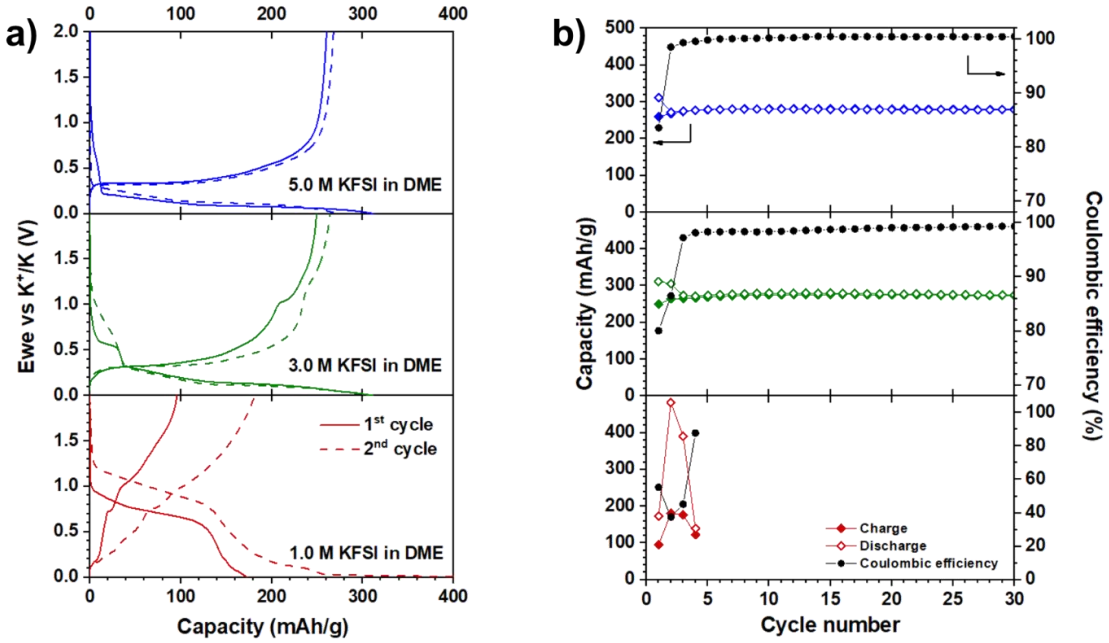


Figure 1. (a) Galvanostatic profiles and (b) capacity as function of cycling of K/graphite half-cells using X M KFSI in DME electrolytes (X = 1.0, 3.0, 5.0)

The above changes and differences can be correlated with a change from co-intercalation to intercalation storage mechanism, as shown by *operando* XRD during the first cycle for the K/graphite half-cells (Figure 2). For all the three cases, the evolution of the diffraction patterns with $K^+$ insertion show typical features of a staging process: the main graphite peak (002) splits into two new peaks, one at lower and one at higher angles, indexed as (00*l*) and (00*l*+1), respectively (Figure 2). No significant changes in the position and intensity of the main graphite peak (002) are observed during the initial part of the discharge (between 1.4 and 1.0 V), implying that in all cases this part of the discharge corresponds to the irreversible decomposition of the electrolyte. At lower potentials, the (002) reflection splits and the (00*l*) and (00*l*+1) peaks shift progressively to lower and higher angles, respectively, indicating the formation of successive graphite intercalation compounds (GICs) through a classical staging process. As the shifts depend on the electrolyte, distinct GICs are formed. Application of Bragg's law allows determining the *l* value and (cf. SI) leads to a small *c* parameter and thus small interlayer spacing between two consecutive graphene sheets for the half-cell with the 5.0 M electrolyte. In contrast, there is a larger *c* parameter and thus a larger interlayer spacing for the half-cell with the 1.0 M electrolyte. At the end of discharge, we observe characteristic peaks centered at 19.25° (5.0 M) and 17.41° (1.0 M) corresponding to *d* spacings of 5.35 and 12.02 Å, respectively. According to previous works, the former corresponds to the typical interlayer distance of $KC_8$ [26,62,63], whereas the latter can be explained only assuming the formation of a co-intercalation phase [19,23–25].

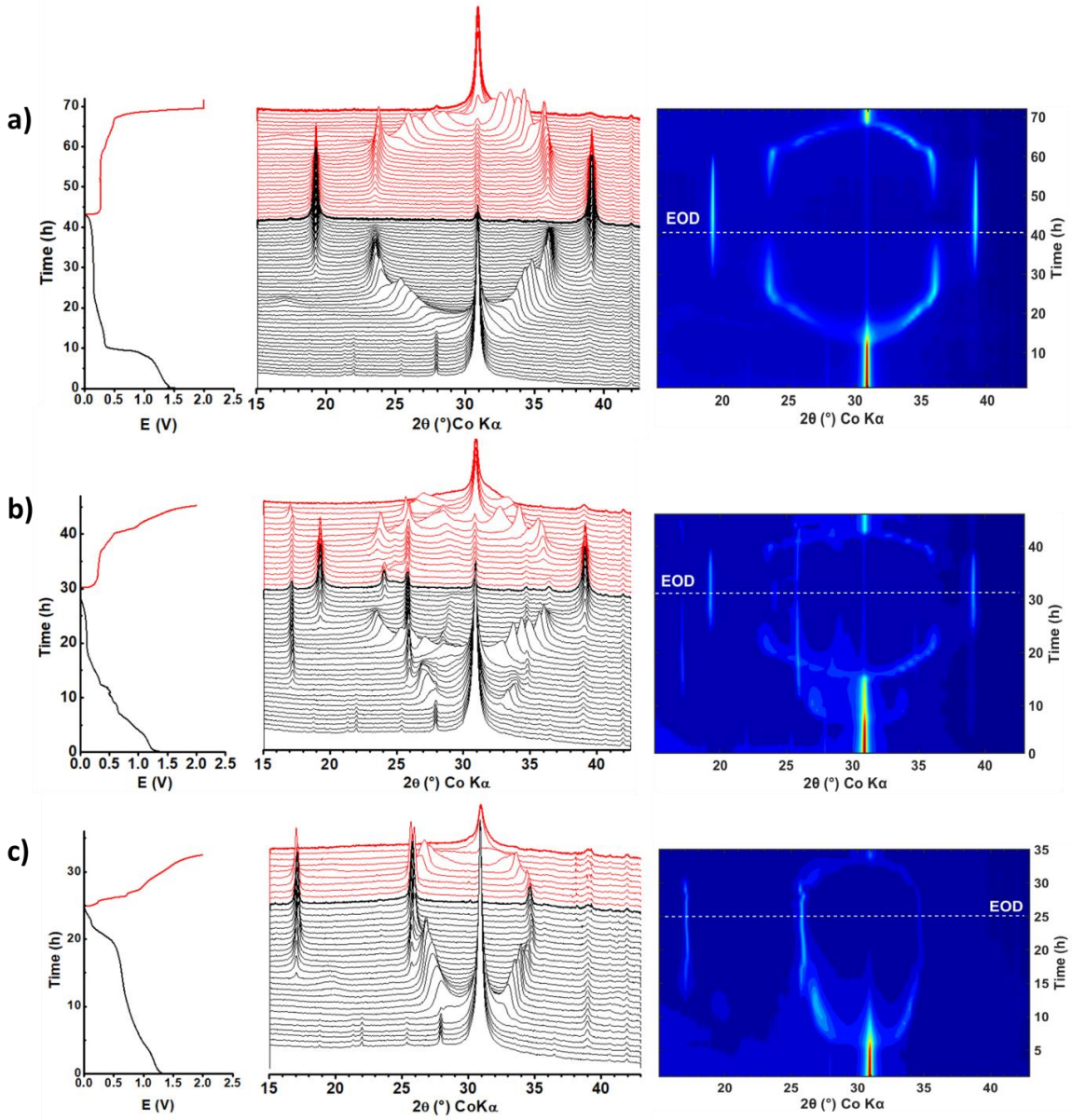


Figure 2. Galvanostatic profiles (left), *operando* XRD diffraction patterns (middle) and contour plots (right) of K/graphite half-cells cycled at 10 mA/g using X M KFSI in DME electrolytes: 5.0 M (a), 3.0 M (b), and 1.0 M (c)

The most interesting case, however, remains that of the intermediate concentrated electrolyte (3.0 M). In this case, (Figure 2b) a staging process resembling that of co-intercalation starting from 0.9 V is observed, and the system has almost finished transitioning from a stage III to a stage II compound.[24]The end member of the co-intercalated phase is completely formed at *ca.* 0.6 V and maintains stable also at lower potentials with respect to the pseudo-leveling surface area and the intensity of its characteristic peak at 17.41° remains until *ca.* 0.1 V (Figure S1b,e). Starting from 0.3 V, the typical features of intercalation appear with the rise of *00l* signal (19.25°) between 0.1 to 0.0 V. Even though the peaks of the co-intercalated species slightly decrease in intensity during $K^+$ intercalation, the main peaks of both intercalated and co-intercalated graphite are observed at the end of discharge (EOD). In the charge, the co-intercalated phase remains unchanged up to *ca.* 1.0 V during which bare $K^+$ ions exit from the host, with similar plateaus resulting in the galvanostatic profiles as well as a similar decrease of the innate peaks in the XRD patterns as observed for the pure mechanism (Figure S1), which confirms the mechanisms being sequential.

In more detail, there is also an additional peak at about 26°, coupled to a peak of weaker intensity at 36.5°, at the end of discharge for the 3.0 M electrolyte. This specific XRD signature, which is not present in the other two systems, might be due to the formation of regularly ordered, alternating, intercalated and co-intercalated layers in a single graphite stack. Indeed, such peaks would correspond to a calculated *d* spacing of 8.59 Å, very close to the average of the values obtained for the 1.0 and 5.0 M electrolytes. Such an average interlayer distance could thus correspond to the formation of alternated intercalated and co-intercalated layers.

Indeed, considering the value of the capacity reached at the end of the co-intercalation process (about 40 mAh/g), the transition from a stage III to a stage II compound should be just about to complete according to the detailed *operando* study of Li *et al*.[24] Therefore, as a stage II compound has already formed during the co-intercalation process, when the intercalation begins at 0.25 V the system cannot undergo the same stacking sequence as seen for the 5.0 M electrolyte, instead the bare $K^+$ must intercalate into the empty layers stacked between layers filled with co-intercalated species. This result, completely new and unexpected as compared to previously published studies, prompted us to investigate the solvation structure of the distinct electrolytes in order to understand the modification of the mechanism as a function of electrolyte salt concentration.

### 3.2. *Cation solvation*

Before addressing in detail the cation solvation in the KFSI/DME system, it is necessary to revisit the conformational population in liquid DME. By applying a Boltzmann distribution (Eq. 1) to pure DME at 20 °C, based on relative electronic energies and entropies (SI), we find TGT to be the dominant conformation, in agreement with the literature [47,64,65]. Furthermore, the TGT and TGG conformers form the most stable complexes with $K^+$, likely due to bidentate chelation by two oxygen atoms (cf. Figure S2). A slightly smaller $\Delta E_{bind}$ of TGG as compared with TGT (1.1 kJ/mol) can be explained by a smaller decrease in the dihedral angle $O_1C_2C_3O_2$ from free to coordinated species (70.8° to 60.4° for TGT, 58.8° to 56.6° for TGG). In contrast, the *trans* position of the oxygen atoms in TTG and TTT only allows for mono-dentate coordination. Finally, despite the preferred *gauche* position of the oxygen atoms in TGG', the steric effect of *g'*-$CH_3$ seems to play a significant role in preventing $K^+$ from being bi-dentately coordinated, why $[K(TGG')]^+$ is the least stable species in this series.

The evolution of the binding energies of the $[K(TGT)_x]^+$ complexes show an increase as function of SN with negligible changes in the average K – O distances for x = 1-4 (Figure 3), while for x = 5 the average K-O distances increases drastically with a large spread. It can be deduced that the optimal SN is 4 and the CN = 8. For x > 4 (e.g., 5), some of the TGT DME solvent may move to the 2$^{nd}$ solvation shell (cf. Figure S3).

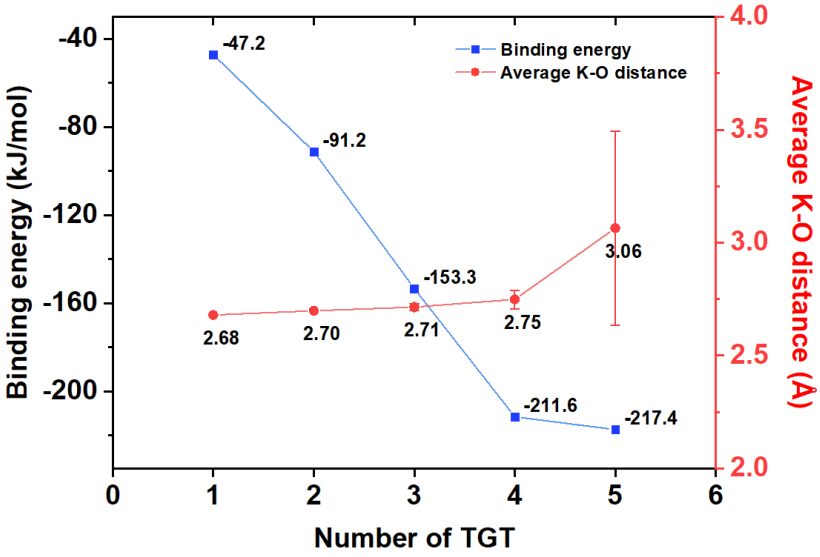


Figure 3. Binding energies and average K-O distances as function of $K^+$-coordinated TGT conformer DME solvents.

In the analysis of the solvates by Raman spectroscopy, the region 800-900 $cm^{-1}$ contains the characteristic vibrations of both free and $K^+$-coordinated DME, ideally also with conformational discrimination, but this region is difficult to analyze due to severe overlaps. By employing the DFT calculations and comparing with deconvoluted spectra, however, the contributions from each conformer to each peak could be unveiled.

First, the deconvoluted Raman spectrum of pure DME (Figure 4) exhibits two strong wide bands at 817 $cm^{-1}$ and 845 $cm^{-1}$ corresponding to the $CH_2$ rocking modes, and some overlapped C–O stretching bands of all conformers [66]. Previous spectroscopic work on DME have ascribed some contribution from TTG and either TTT or TGG'[66,67], but our DFT calculations indicate that only the conformers having their oxygen atoms at *gauche* position (TGG, TGG' and TGT) exhibit strong Raman activities, while TTT and TTG have non or negligibly small activities (cf. Table S2). Therefore, the latter are disregarded. On the other hand, each of the three species TGG, TGG' and TGT possesses two strong Raman vibrations in this region: one is the symmetrical $CH_2$ rocking mode, and the other could be either an asymmetrical $CH_2$ rocking mode (TGG' and TGT) or the combination of different vibrations (TGG). While these vibrations of TGG and TGG' have different Raman shifts, those of TGT seem to have the same. Additionally, the minute errors (*ca.* 1%) show a very good agreement between the (scaled) calculated frequencies [54] and the experimental data (cf. Table S2). From this, the peak at 817 $cm^{-1}$ is assigned to TGG and TGG', and the peak at 845 $cm^{-1}$ to TGG, TGG' and TGT.

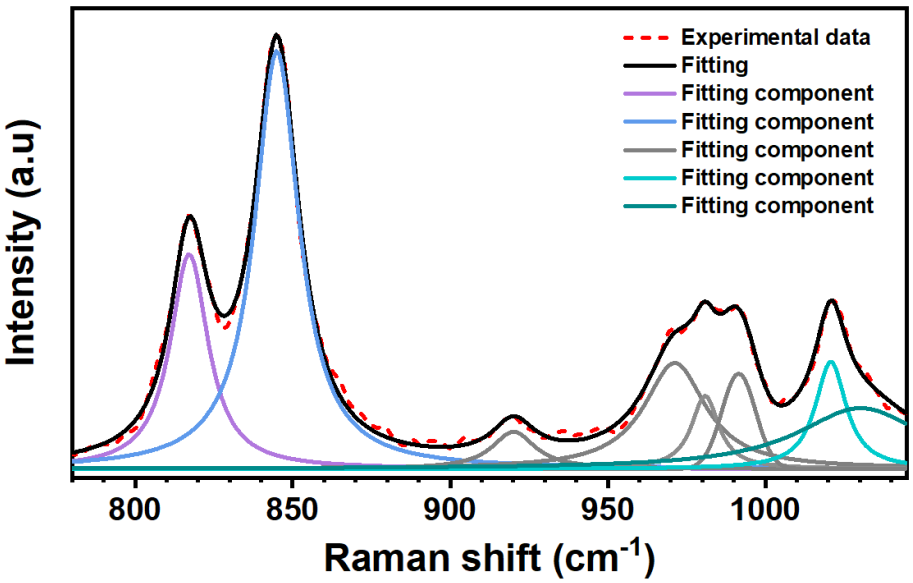

Figure 4. Deconvoluted Raman spectrum of pure DME in the region of 780 – 1045 $cm^{-1}$.

The effect of KFSI in DME can be observed by following Raman spectra of the electrolytes with increasing salt concentration (Figure 5). Based on assignments previously set for LiFSI [68] and for glyme-based electrolytes [45,46,69], the deconvoluted KFSI-DME spectra have; contributions at 717, 727 and 737 $cm^{-1}$ that are assigned to free FSI anions (or solvent-separated ion-pairs, SSIPs), CIPs of K-FSI, and AGGs, respectively; contributions at 817 and 845 $cm^{-1}$ from free DME; and, finally, contributions at 827 and 855 $cm^{-1}$ from coordinated DME in the TGT conformation (cf. Figure S4). The large right-tailing peak at 700–780 $cm^{-1}$ results from the S–N stretching mode of FSI anions [21,68,70–72]. As the salt concentration increases, the peak exhibits a blue shift, indicating the formation of CIPs and/or AGGs. Based on the evolution of fitted peak intensities, we divide *the plot* into two regions: low concentration (LC) region (< 5.0 M, or DME:KFSI > 2), and high concentration (HC) region (≥ 5.0 M). In the LC region, even in the most dilute electrolytes (< 1.0 M) CIPs exists, but free FSI is the dominant anion species. With increasing salt concentration, the proportion of free FSI follows a parabolic function (Figure S3), while the CIPs increase. When DME:KFSI ≥ 3, the AGGs increase and become dominant in the HC region. A small amount of free FSI anions still exists in the 5.0 M electrolyte, but disappear when more salt is added.

In the DME region, the peak at 817 $cm^{-1}$ decreases and this could be due to less free TGG and TGG', as two new peaks at 827 and 855 $cm^{-1}$ increase as function of salt concentration (Figure 4b). Indeed, Hosaka *et al.* [45] concluded the latter to come from coordinated DME and Liu *et al.* [46] assigned them to C–O bonds in DME coordinated to $K^+$ without any contribution from the $CH_2$ groups. In contrast, we believe that both $CH_2$ and C–O groups contribute (Table S3) also as the calculated Raman activities (Table S2) suggests assignment to $CH_2$ rocking mode solely or mixed with C–O stretching vibrations of coordinated DME in TGT conformation, respectively. In contrast to the gradual reduction of the peak at 817 $cm^{-1}$, the peak at 845 $cm^{-1}$ seems to be unchanged in the LC region and then slightly decreases at higher concentrations (Figure S5). According to our DFT data, there are two possible solvate types, by TGT and TGG, respectively, as their binding energies are very close. The vibrational modes of TGG at 817 and 845 $cm^{-1}$ are not shifted upon coordination (Table S2), which makes coordinated TGG hard to discern. The Raman activity of the vibration at 845 $cm^{-1}$ of coordinated TGG is much stronger than that at 817 $cm^{-1}$, and while the peak at 817 $cm^{-1}$ only has contributions from free and coordinated TGG, the peak at 845 also has contributions from free TGT

and hence the different evolutions of these peaks. However, as the absolute population of TGG is much lower than TGT, we consider $[K(TGT)_x]^+$ to be the major cation solvate species.

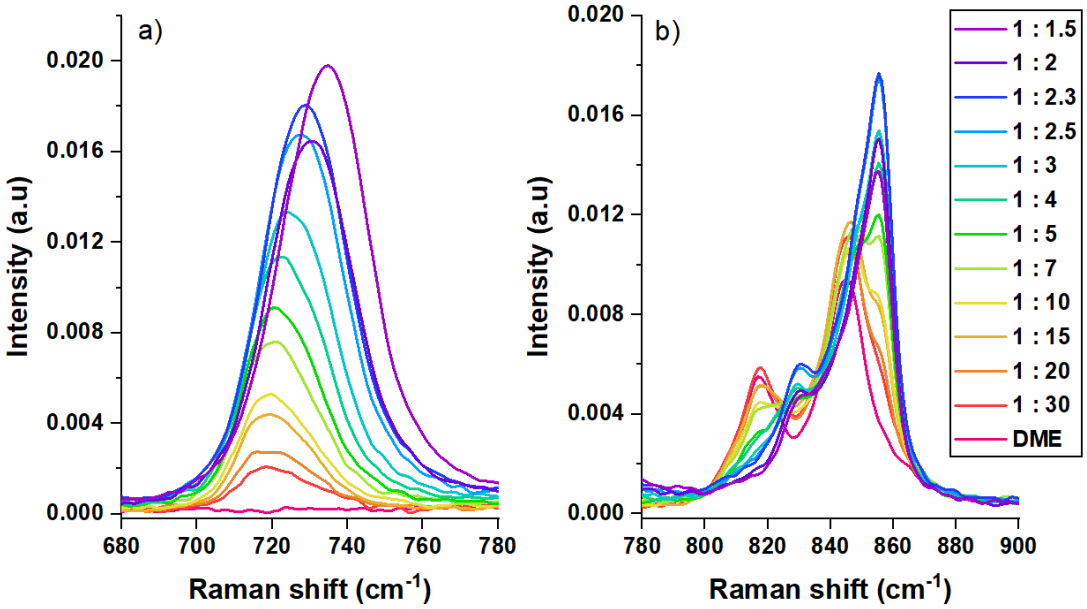


Figure 5. Raman spectra of pure DME and electrolytes: (a) the S–N stretching mode of FSI, and (b) the $CH_2$ rocking modes of DME.

The evolution of the peaks assigned as coordinated TGT at 855 and 830 $cm^{-1}$ (cf. Figure S6) show the same trend: both increase linearly as function of salt concentration up to a KFSI:DME = 1:2.3 ratio, after which they decrease again. Artificial spectra of $[K(TGT)_x]^+$ complexes show that the peak positions negligibly change and the Raman activities to be linear functions of the number of coordinated DME in TGT conformation (cf. Figure S7). We deduce that these peaks have the same origin, *i.e.*, $[K(TGT)_x]^+$. In the LC region, the peak intensities are linear functions of the molar fraction of KFSI, which means that the average SN is almost constant, but in the HC region the peak intensities decrease, hence reduced SNs.

From the above, a statistical combination of DFT calculated data and experimental spectroscopy data was applied to calculate the SN; the intensity of each peak in the region 780–1045 $cm^{-1}$ was calculated by the equation:

$$I_{peak} = m \times \sum n_i \times a_i \qquad (2)$$

where, $I_{peak}$ is the fitted peak intensity, $n_i$ and $a_i$ are the populations and computed Raman activities of conformer *i*, and *m* is an adjusting factor, on average $4.6\ 10^{-4} \pm 2.4\ 10^{-4}$ (cf. Table S3). Since the intensity of the peak at 855 $cm^{-1}$ is a linear function of the salt molar fraction, this can be obtained as:

$$\begin{aligned} I_{855} &= \left(a_{855} \times n_{tgt-b}\right) \times m + k \\ &= \left(a_{855} \times SN_{tgt} \times m\right) \times n_{KFSI} + k \end{aligned} \qquad (3)$$

where $n_{tgt\text{-}b}$ is the molar fraction of bound TGT, $n_{KFSI}$ is the molar fraction of KFSI; $a_{855}$ is the calculated Raman activity of the $[K(TGT)]^+$ complex, and *k* is the intercept. The SN, deduced from the slope (Figure 6) is **2.7**, which is equivalent to the formation of approximately 30% $[K(TGT)_2]^+$ and 70% $[K(TGT)_3]^+$. This agrees very well with the binding energies, were the addition of the third TGT lowers the energy the most. In the HC region the SN is strongly reduced; for DME:KFSI = 2.0 and 1.5 the SNs are 1.9 and 1.4, respectively.

The evolution of the SNs as a function of salt concentration also provides a convincing explanation for the mixed mechanism of graphite using the 3.0 M electrolyte. As this electrolyte stays in the LC region, the $K^+$ ions are surrounded by 2 or 3 solvent molecules, which leads to the co-intercalation at the beginning of the discharge process. Consequently, the salt-to-solvent molar ratio in the bulk rises, and the concentration of the electrolyte becomes higher. As a result, the SN of $K^+$ reduces, and the intercalation takes place at low potentials.

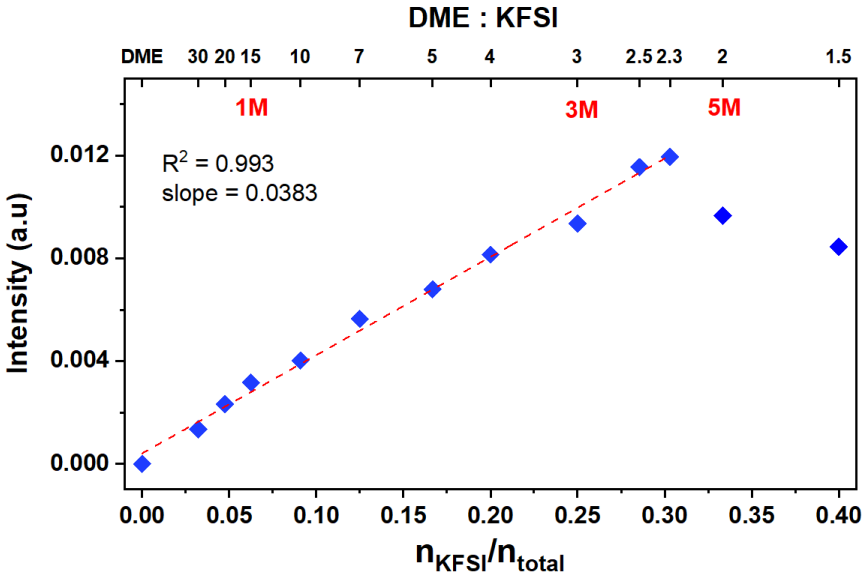


Figure 6. Evolution of the 855 $cm^{-1}$ deconvoluted peak as a function of the salt molar fraction.

### 3.3. *Origin of (co)intercalation/intercalation and insight into the storage mechanism*

From the literature extremely thin SEI films are expected for glyme-based electrolytes in alkali-metal systems, why co-intercalation of $K^+$-DME complexes would be expected to be independent of the electrolyte salt concentration. Differences in the storage mechanism, however, from co-intercalation to intercalation with increasing KFSI concentration could depend upon specific properties of the SEI, and a stable and uniform SEI with a high content of inorganic components is expected to be formed in HCEs [73].

To better understand whether the change in storage mechanism depends on the specific nature of the SEI formed or on the properties of the electrolytes themselves, two additional tests were performed: *i)* a graphite electrode underwent a full discharge/charge (pre)cycling *vs.* K with the 5.0 M KFSI in DME electrolyte and then put and cycled in a new cell with the 1.0 M KFSI in DME electrolyte, and *ii)* a second cell prepared *vice-versa* (Figure 7).

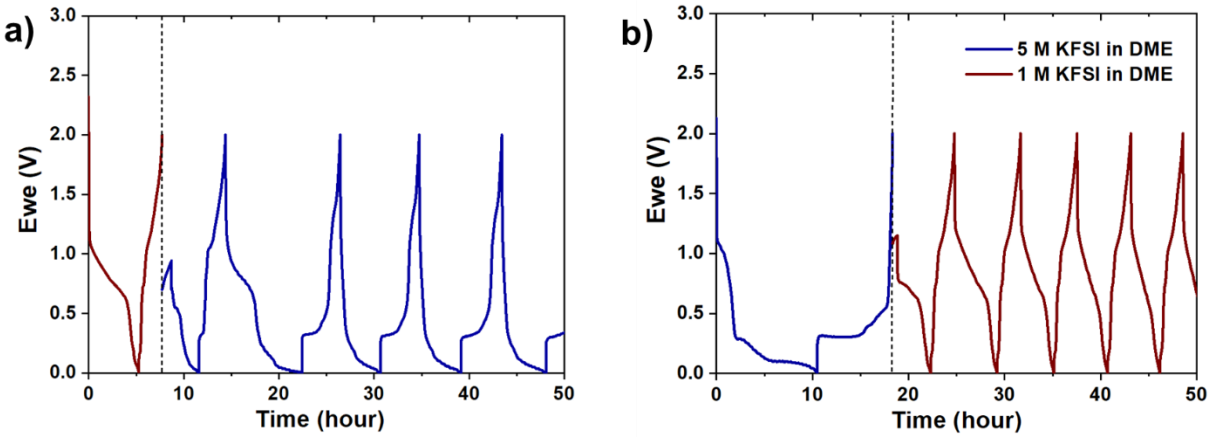

Figure 7. Changes in storage mechanism as observed by cycling pre-cycled cells with different KFSI in DME electrolytes: (a) from 1.0 to 5.0 M and (b) from 5.0 to 1.0 M.

For the cell pre-cycled with the 1.0 M electrolyte, there is a gradual disappearance of co-intercalation in favor of intercalation with the fresh 5.0 M electrolyte. Almost the same easy change in mechanism, but in the reverse direction, when moving from the 5.0 to the 1.0 M electrolyte, indicates that the different SEIs most probably are not responsible for the changed mechanism. If a stable SEI were formed in the first experiment, co-intercalation would not be observed immediately, but more intriguing is that in the second cell co-intercalation seems to be retained for one additional cycle. This can be explained by considering that either the SEI formed is more stable, taking some time to dissolve and thereafter form a new SEI, or most probably that some trace of co-intercalation is retained by graphite, possibly involving the SEI formed. Indeed, previous work on Na-based systems [36,74] clearly indicate that even when it has been completely desodiated, graphite still shows some volume expansion as compared to its pristine state, probably due to the presence of some solvent molecules trapped in the interlayer spacing. In the same direction goes the study of Aurbach and co-workers, which showed by NMR spectroscopy that about 25% of diglyme to be retained inside graphite after desodiation [75]. Therefore, even if additional investigations are needed to completely understand both the composition and importance of the SEI on the long-term cycling performance of graphite in these KIBs, the SEI does not seem directly responsible for the observed storage mechanism(s).

This means that we now can turn our eye to the $K^+$ solvation and speciation, and from the above the intercalation/co-intercalation can be described by this general reaction:

$$C_n + K^+ + e^- + v\ DME \rightarrow C_n^-(DME)_vK^+ \quad (4)$$

In a typical KIB full cell working with intercalation in both electrodes, the average concentration of $K^+$ in the electrolyte is constant. In the case of co-intercalation, however, there will be a net increase in the average $K^+$ concentration, since the solvent (concentration) outside the electrodes decreases. In a typical coin-cell, with a hundred microliters of electrolyte and a few milligrams of graphite electrode, this solvent depletion becomes significant, especially for HCEs. This would result in a further decrease in the SN and is a reasonable explanation for the changed storage mechanism.

A support for this proposal is the mixed mechanism observed for the intermediate 3.0 M electrolyte; being at the border between the LC and HC regions, the co-intercalation observed initially leads to reduced DME available in the electrolyte, and the mechanism is converted to intercalation.

From a thermodynamic point-of-view, the potential differences between intercalation and co-intercalation processes can be studied. As the $K^+$ first solvation shell is either completely removed or not before the very entering into graphite, the energy difference should be related to the desolvation

energy of the intercalated $[K(TGT)_x]^+$ complex. Based on the *operando* XRD patterns (Figure 2), the starting potentials are 0.33 and 0.86 V, respectively, *i.e.*, ΔE = 0.53 V, and the corresponding difference in Gibbs free energy (ΔG) estimated from:

$$\Delta G = nF\Delta E \qquad (5)$$

where *n* is the number of electrons transferred. The ΔG obtained is of the order of 50 kJ/mol, which indeed is of the order of the binding energy of one TGT to $K^+$. This means that a reduction of the SN of $K^+$ in DME by ca. one unit, occurring in the case of co-intercalation, could be disfavoured, in terms of energy, with respect to a change in the storage mechanism to intercalation.

To probe further the interactions and provide plausible configurations inside the interlayer spacing, MC simulations were performed starting from a composition of $K(DME)_xC_{11}$, as extrapolated from the 1.0 M-to-5.0 M discharge capacity ratio of graphite in the second cycle (Fig 1a). The density of DME and $K^+$ inside the interlayer spacing and the distances show saturation for a ratio DME:$K^+$ of 1.35:1 (Figure 8). The $K^+$ cations seem to be strongly interacting with the graphene layers and the presence of DME does not change this, as previously observed for $Na^+$-saturated graphite in interaction with DME [40] as well as for other alkali cations [76]. All distances are between 2.5 and 2.7 Å, in agreement with the DFT results.

The impact of confinement on the DME molecules in the interlayer spacing was studied by the adsorption enthalpy. $K^+$ in the presence of 1 DME molecule, without any graphene layers, results in 76 kJ/mol, in general agreement with previous DFT calculations for $Na^+$ [77], but slightly higher as no solvent is taken into account here. In contrast, the adsorption enthalpy is 110 kJ/mol showing the strong effect of the confinement.

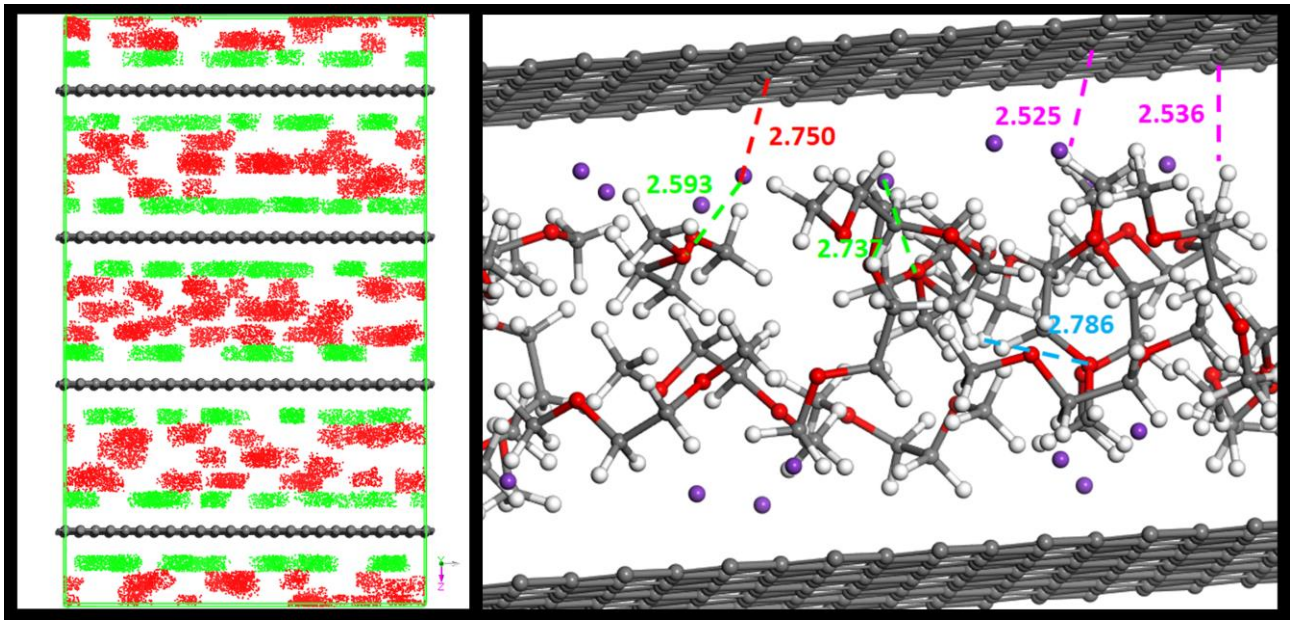


Figure 8. Density of presence (red points correspond to DME and green points to $K^+$) and snapshots of the main distances in the $K(DME)_xC_{11}$ structure in presence of DME at saturation obtained from MC simulations. The distances reported in red, green, cyan and pink correspond to the distances between cations and layers, DME and cations, DME molecules, and DME and layers respectively.

## 4. Summary

The electrochemical storage mechanisms of $K^+$ in graphite using KFSI:DME electrolytes of high and low salt concentrations have been unambiguously distinguished by using *operando* XRD. The cation solvation was identified to be the key factor determining the storage mechanism, as the SEIs formed

were found to be unable to block co-intercalation regardless of the electrolyte salt concentration. The binding energies of $[K(DME)_x]^+$ complexes revealed the selectivity in conformational solvation as well as confirmed that the highest SN by DME is 4, corresponding to a maximum CN = 8. Yet, SNs of 2 and 3 by DME are dominant for the less concentrated electrolytes, leading to difficult desolvation, where co-intercalation occurs. At higher salt concentrations, with SNs ≤ 2, intercalation becomes energetically favored and this renders the HCEs the superior alternative, both in terms of thermodynamics and kinetics, for graphite-based anodes in KIBs. The strong influence of the electrolyte salt concentration on the charge storage mechanism of $K^+$ in graphite paves the way for better design of electrolytes for the emerging field of KIBs.

**Acknowledgements**

This work was supported by a public grant overseen by the French National Research Agency (ANR) as part of the "Investissements d'Avenir" programme (Project ANR-10-LABX- 76-01 (Labex STOREX)). The Alistore-European Research Institute (ALISTORE-ERI) network is warmly thanked for funding the PhD grant of P. N. Le Pham. Access to the Analysis and Characterization platform of "Pôle Chimie Balard" (PAC-Balard) is gratefully acknowledged. G. Å. acknowledges the Swedish Energy Agency for support thought the projects within "Batterifondsprogrammet": "Next Generation Batteries" (Grant No. 37671-1) and "Highly Concentrated Electrolytes" (Grant No. 39909-1), and the EU H2020 NAIADES Project (LCE10-2014, No. 646433). Finally, we acknowledge the computational resources provided by the Swedish National Infrastructure for Computing (SNIC) at Chalmers Center for Computational Science and Engineering ($C^3$SE).

**References**

[1] Z. Yang, J. Zhang, M. C. W. Kintner-Meyer, X. Lu, D. Choi, J. P. Lemmon, J. Liu, Electrochemical Energy Storage for Green Grid, Chem. Rev. 111 (2011) 3577–3613. https://doi.org/10.1021/cr100290v.

[2] B. Dunn, H. Kamath, J.-M.M. Tarascon, Electrical energy storage for the grid: A battery of choices, Science (80-. ). 334 (2011) 928–935. https://doi.org/10.1126/science.1212741.

[3] M. Armand, J.-M. Tarascon, Building better batteries, Nature. 451 (2008) 652. http://dx.doi.org/10.1038/451652a.

[4] M. Stanley Whittingham, Lithium Batteries and Cathode Materials, Chem. Rev. 104 (2004) 4271–4302. https://doi.org/10.1021/cr020731c.

[5] D. Larcher, J.-M. Tarascon, Towards greener and more sustainable batteries for electrical energy storage, Nat. Chem. 7 (2015) 19–29. https://doi.org/10.1038/nchem.2085.

[6] T. Hosaka, K. Kubota, A.S. Hameed, S. Komaba, Research Development on K-Ion Batteries, Chem. Rev. 120 (2020) 6358–6466. https://doi.org/10.1021/acs.chemrev.9b00463.

[7] S.M. Ahmed, G. Suo, W.A. Wang, K. Xi, S. Bin Iqbal, Improvement in potassium ion batteries electrodes: recent developments and efficient approaches, J. Energy Chem. 62 (2021) 307–337. https://doi.org/10.1016/j.jechem.2021.03.032.

[8] J. Hui, N.B. Schorr, S. Pakhira, Z. Qu, J.L. Mendoza-Cortes, J. Rodríguez-López, Achieving Fast and Efficient K+ Intercalation on Ultrathin Graphene Electrodes Modified by a Li+ Based Solid-Electrolyte Interphase, J. Am. Chem. Soc. 140 (2018) 13599–13603. https://doi.org/10.1021/jacs.8b08907.

[9] H. Ding, J. Zhou, A.M. Rao, B. Lu, Cell-like-carbon-micro-spheres for robust potassium anode, Natl. Sci. Rev. 8 (2021) nwaa276. https://doi.org/10.1093/nsr/nwaa276.

[10] Q. Zhang, X. Cheng, C. Wang, A.M. Rao, B. Lu, Sulfur-assisted large-scale synthesis of

graphene microspheres for superior potassium-ion batteries, 14 (2021) 965–974.

[11] H. Chen, P. He, M. Li, Y. Wen, G. Cao, J. Qiu, H. Ming, P. Zhao, Life and High-Energy-Density Lithium-Ion Batteries, (2021). https://doi.org/10.1021/acsaem.1c00808.

[12] Z. Jian, W. Luo, X. Ji, Carbon Electrodes for K-Ion Batteries, J. Am. Chem. Soc. 137 (2015) 11566–11569. https://doi.org/10.1021/jacs.5b06809.

[13] J. Zhao, X. Zou, Y. Zhu, Y. Xu, C. Wang, Electrochemical Intercalation of Potassium into Graphite, Adv. Funct. Mater. 26 (2016) 8103–8110. https://doi.org/10.1002/adfm.201602248.

[14] W. Luo, J. Wan, B. Ozdemir, W. Bao, Y. Chen, J. Dai, H. Lin, Y. Xu, F. Gu, V. Barone, L. Hu, Potassium Ion Batteries with Graphitic Materials, Nano Lett. 15 (2015). https://doi.org/10.1021/acs.nanolett.5b03667.

[15] Y. An, H. Fei, G. Zeng, L. Ci, B. Xi, S. Xiong, J. Feng, Commercial expanded graphite as a low–cost, long-cycling life anode for potassium–ion batteries with conventional carbonate electrolyte, J. Power Sources. 378 (2018) 66–72. https://doi.org/10.1016/j.jpowsour.2017.12.033.

[16] L. Fan, R. Ma, Q. Zhang, X. Jia, B. Lu, Graphite Anode for a Potassium-Ion Battery with Unprecedented Performance, Angew. Chem. Int. Ed. 58 (2019) 10500–10505. https://doi.org/10.1002/anie.201904258.

[17] M. Carboni, A.J. Naylor, M. Valvo, R. Younesi, Unlocking high capacities of graphite anodes for potassium-ion batteries, RSC Adv. 9 (2019) 21070–21074. https://doi.org/10.1039/c9ra01931f.

[18] L. Wang, J. Yang, J. Li, T. Chen, S. Chen, Z. Wu, J. Qiu, B. Wang, P. Gao, X. Niu, H. Li, Graphite as a potassium ion battery anode in carbonate-based electrolyte and ether-based electrolyte, J. Power Sources. 409 (2019) 24–30. https://doi.org/10.1016/j.jpowsour.2018.10.092.

[19] X. Niu, L. Li, J. Qiu, J. Yang, J. Huang, Z. Wu, J. Zou, C. Jiang, J. Gao, L. Wang, Salt-concentrated electrolytes for graphite anode in potassium ion battery, Solid State Ionics. 341 (2019) 1–6. https://doi.org/10.1016/j.ssi.2019.115050.

[20] L. Qin, N. Xiao, J. Zheng, Y. Lei, D. Zhai, Y. Wu, Localized High-Concentration Electrolytes Boost Potassium Storage in High-Loading Graphite, Adv. Energy Mater. 9 (2019) 1902618. https://doi.org/10.1002/aenm.201902618.

[21] N. Xiao, W.D. Mcculloch, Y. Wu, Reversible Dendrite-Free Potassium Plating and Stripping Electrochemistry for Potassium Secondary Batteries, J. Am. Chem. Soc. 139 (2017) 9475–9478. https://doi.org/10.1021/jacs.7b04945.

[22] J. Touja, P.N. Le Pham, N. Louvain, L. Monconduit, L. Stievano, Effect of the electrolyte on the K-metal batteries, Chem. Commun. 56 (2020) DOI: 10.1039/D0CC05024E. https://doi.org/10.1039/D0CC05024E.

[23] A.P. Cohn, N. Muralidharan, R. Carter, K. Share, L. Oakes, C.L. Pint, Durable potassium ion battery electrodes from high-rate cointercalation into graphitic carbons, J. Mater. Chem. A. 4 (2016) 14954–14959. https://doi.org/10.1039/c6ta06797b.

[24] L. Li, L. Liu, Z. Hu, Y. Lu, Q. Liu, S. Jin, Q. Zhang, S. Zhao, S.L. Chou, Understanding High-Rate K+-Solvent Co-Intercalation in Natural Graphite for Potassium-Ion Batteries, Angew. Chemie - Int. Ed. 59 (2020) 12917–12924. https://doi.org/10.1002/anie.202001966.

[25] H. Kim, G. Yoon, K. Lim, K. Kang, A comparative study of graphite electrodes using the co-intercalation phenomenon for rechargeable Li, Na and K batteries, Chem. Commun. 52 (2016) 12618–12621. https://doi.org/10.1039/c6cc05362a.

[26] Y. Li, Y. Lu, P. Adelhelm, M.-M.M. Titirici, Y.-S.S. Hu, Intercalation chemistry of graphite: Alkali metal ions and beyond, Chem. Soc. Rev. 48 (2019) 4655–4687. https://doi.org/10.1039/c9cs00162j.

[27] H.H. Kim, J. Hong, G. Yoon, H.H. Kim, K.Y. Park, M.S. Park, W.S. Yoon, K. Kang, Sodium

intercalation chemistry in graphite, Energy Environ. Sci. 8 (2015) 2963–2969. https://doi.org/10.1039/c5ee02051d.

[28] L. Seidl, N. Bucher, E. Chu, S. Hartung, S. Martens, O. Schneider, U. Stimming, Intercalation of solvated Na-ions into graphite, Energy Environ. Sci. 10 (2017) 1631–1642. https://doi.org/10.1039/c7ee00546f.

[29] X. Zhang, F. Hao, Y. Cao, Y. Xie, S. Yuan, X. Dong, Y. Xia, Dendrite-Free and Long-Cycling Sodium Metal Batteries Enabled by Sodium-Ether Cointercalated Graphite Anode, Adv. Funct. Mater. 2009778 (2021) 2009778. https://doi.org/10.1002/adfm.202009778.

[30] H. Kim, J. Hong, Y.U. Park, J. Kim, I. Hwang, K. Kang, Sodium storage behavior in natural graphite using ether-based electrolyte systems, Adv. Funct. Mater. 25 (2015) 534–541. https://doi.org/10.1002/adfm.201402984.

[31] L. Zhang, W. Wang, S. Lu, Y. Xiang, Carbon Anode Materials: A Detailed Comparison between Na-ion and K-ion Batteries, Adv. Energy Mater. 2003640 (2021) 1–15. https://doi.org/10.1002/aenm.202003640.

[32] H. Zhang, Y. Yang, D. Ren, L. Wang, X. He, Graphite as anode materials : Fundamental mechanism , recent progress and advances, Energy Storage Mater. 36 (2021) 147–170. https://doi.org/10.1016/j.ensm.2020.12.027.

[33] K. Xu, Electrolytes and interphases in Li-ion batteries and beyond, Chem. Rev. 114 (2014) 11503–11618. https://doi.org/10.1021/cr500003w.

[34] B. Jache, J.O. Binder, T. Abe, P. Adelhelm, A comparative study on the impact of different glymes and their derivatives as electrolyte solvents for graphite co-intercalation electrodes in lithium-ion and sodium-ion batteries, Phys. Chem. Chem. Phys. 18 (2016) 14299–14316. https://doi.org/10.1039/c6cp00651e.

[35] H. Kim, K. Lim, G. Yoon, J.H. Park, K. Ku, H.D. Lim, Y.E. Sung, K. Kang, Exploiting Lithium–Ether Co-Intercalation in Graphite for High-Power Lithium-Ion Batteries, Adv. Energy Mater. 7 (2017) 1–10. https://doi.org/10.1002/aenm.201700418.

[36] M. Liu, L. Xing, K. Xu, H. Zhou, J. Lan, C. Wang, W. Li, Deciphering the paradox between the Co-intercalation of sodium-solvent into graphite and its irreversible capacity, Energy Storage Mater. 26 (2020) 32–39. https://doi.org/10.1016/j.ensm.2019.12.026.

[37] B. Jache, P. Adelhelm, Use of graphite as a highly reversible electrode with superior cycle life for sodium-ion batteries by making use of co-intercalation phenomena, Angew. Chemie - Int. Ed. 53 (2014) 10169–10173. https://doi.org/10.1002/anie.201403734.

[38] M. Goktas, C. Bolli, E.J. Berg, P. Novák, K. Pollok, F. Langenhorst, M. v. Roeder, O. Lenchuk, D. Mollenhauer, P. Adelhelm, Graphite as Cointercalation Electrode for Sodium-Ion Batteries: Electrode Dynamics and the Missing Solid Electrolyte Interphase (SEI), Adv. Energy Mater. 8 (2018) 1702724. https://doi.org/10.1002/aenm.201702724.

[39] K. Westman, R. Dugas, P. Jankowski, W. Wieczorek, G. Gachot, M. Morcrette, E. Irisarri, A. Ponrouch, M.R. Palacín, J.-M. Tarascon, P. Johansson, Diglyme Based Electrolytes for Sodium-Ion Batteries, ACS Appl. Energy Mater. 1 (2018) 2671–2680. https://doi.org/10.1021/acsaem.8b00360.

[40] S.C. Jung, Y.-J. Kang, Y.-K. Han, Origin of excellent rate and cycle performance of Na+-solvent cointercalated graphite vs. poor performance of Li+-solvent case, Nano Energy. 34 (2017) 456–462. https://doi.org/10.1016/j.nanoen.2017.03.015.

[41] X. Zhang, J. Meng, X. Wang, Z. Xiao, P. Wu, L. Mai, Comprehensive Insights into Electrolytes and Solid Electrolyte Interfaces in Potassium-Ion Batteries, Energy Storage Mater. 38 (2021) 30–49. https://doi.org/10.1016/j.ensm.2021.02.036.

[42] M. Gu, L. Fan, J. Zhou, A.M. Rao, B. Lu, Regulating Solvent Molecule Coordination with KPF 6 for Superstable Graphite Potassium Anodes , ACS Nano. 15 (2021) 9167–9175. https://doi.org/10.1021/acsnano.1c02727.

[43] G. Åvall, J. Wallenstein, G. Cheng, K.L. Gering, P. Johansson, D.P. Abraham, Highly Concentrated Electrolytes : Electrochemical and Physicochemical Characteristics of LiPF 6 in Propylene Carbonate Solutions Highly Concentrated Electrolytes : Electrochemical and Physicochemical Characteristics of LiPF 6 in Propylene Carbonate Solut, (2021). https://doi.org/10.1149/1945-7111/abfdc3.

[44] G. Yoon, H. Kim, I. Park, K. Kang, Conditions for Reversible Na Intercalation in Graphite: Theoretical Studies on the Interplay Among Guest Ions, Solvent, and Graphite Host, Adv. Energy Mater. 7 (2017). https://doi.org/10.1002/aenm.201601519.

[45] T. Hosaka, T. Matsuyama, K. Kubota, R. Tatara, S. Komaba, KFSA/glyme electrolytes for 4 V-class K-ion batteries, J. Mater. Chem. A. 8 (2020) 23766–23771. https://doi.org/10.1039/d0ta08851j.

[46] X. Liu, G.A. Elia, X. Gao, B. Qin, H. Zhang, S. Passerini, Highly Concentrated KTFSI : Glyme Electrolytes for K/Bilayered-V 2 O 5 Batteries, Batter. Supercaps. (2020) 1–8. https://doi.org/10.1002/batt.202000003.

[47] N. Goutev, K. Ohno, H. Matsuura, Raman spectroscopic study on the conformation of 1,2-dimethoxyethane in the liquid phase and in aqueous solutions, J. Phys. Chem. A. 104 (2000) 9226–9232. https://doi.org/10.1021/jp001340+.

[48] M. Morcrette, Y. Chabre, G.B.M. Vaughan, G.G. Amatucci, J.-B. Leriche, S. Patoux, C. Masquelier, J.-M. Tarascon, In situ X-ray diffraction techniques as a powerful tool to study battery electrode materials, Electrochim. Acta. 47 (2002) 3137–3149. https://doi.org/10.1016/S0013-4686(02)00233-5.

[49] M.J. Frisch, G.W. Trucks, H.B. Schlegel, G.E. Scuseria, M.A. Robb, J.R. Cheeseman, G. Scalmani, V. Barone, G.A. Petersson, H. Nakatsuji, X. Li, M. Caricato, A. V Marenich, J. Bloino, B.G. Janesko, R. Gomperts, B. Mennucci, H.P. Hratchian, J. V Ortiz, A.F. Izmaylov, J.L. Sonnenberg, D. Williams-Young, F. Ding, F. Lipparini, F. Egidi, J. Goings, B. Peng, A. Petrone, T. Henderson, D. Ranasinghe, V.G. Zakrzewski, J. Gao, N. Rega, G. Zheng, W. Liang, M. Hada, M. Ehara, K. Toyota, R. Fukuda, J. Hasegawa, M. Ishida, T. Nakajima, Y. Honda, O. Kitao, H. Nakai, T. Vreven, K. Throssell, J.A. Montgomery Jr., J.E. Peralta, F. Ogliaro, M.J. Bearpark, J.J. Heyd, E.N. Brothers, K.N. Kudin, V.N. Staroverov, T.A. Keith, R. Kobayashi, J. Normand, K. Raghavachari, A.P. Rendell, J.C. Burant, S.S. Iyengar, J. Tomasi, M. Cossi, J.M. Millam, M. Klene, C. Adamo, R. Cammi, J.W. Ochterski, R.L. Martin, K. Morokuma, O. Farkas, J.B. Foresman, D.J. Fox, Gaussian 16, Revision .03, (2016).

[50] Y. Zhao, D.G. Truhlar, The M06 suite of density functionals for main group thermochemistry, thermochemical kinetics, noncovalent interactions, excited states, and transition elements: Two new functionals and systematic testing of four M06-class functionals and 12 other function, Theor. Chem. Acc. 120 (2008) 215–241. https://doi.org/10.1007/s00214-007-0310-x.

[51] J. Tomasi, B. Mennucci, R. Cammi, Quantum mechanical continuum solvation models, Chem. Rev. 105 (2005) 2999–3093. https://doi.org/10.1021/cr9904009.

[52] M.D. Hanwell, D.E. Curtis, D.C. Lonie, T. Vandermeersch, E. Zurek, G.R. Hutchison, Avogadro: an advanced semantic chemical editor, visualization, and analysis platform, J. Cheminform. 4 (2012) 17. https://doi.org/10.1186/1758-2946-4-17.

[53] N.M. O'boyle, A.L. Tenderholt, K.M. Langner, cclib: A library for package-independent computational chemistry algorithms, J. Comput. Chem. 29 (2008) 839–845. https://doi.org/https://doi.org/10.1002/jcc.20823.

[54] D.O. Kashinski, G.M. Chase, R.G. Nelson, O.E. Di Nallo, A.N. Scales, D.L. Vanderley, E.F.C. Byrd, Harmonic Vibrational Frequencies: Approximate Global Scaling Factors for TPSS, M06, and M11 Functional Families Using Several Common Basis Sets, J. Phys. Chem. A. 121 (2017) 2265–2273. https://doi.org/10.1021/acs.jpca.6b12147.

[55] A.K. Rappe, C.J. Casewit, K.S. Colwell, W.A. Goddard, W.M. Skiff, UFF, a full periodic table

force field for molecular mechanics and molecular dynamics simulations, J. Am. Chem. Soc. 114 (1992) 10024–10035. https://doi.org/10.1021/ja00051a040.

[56] D. Frenkel, B. Smit, Understanding Molecular Simulation, Elsevier, 2002. https://doi.org/10.1016/b978-0-12-267351-1.x5000-7.

[57] M. Goktas, C. Bolli, J. Buchheim, E.J. Berg, P. Novák, F. Bonilla, T. Rojo, S. Komaba, K. Kubota, P. Adelhelm, Stable and Unstable Diglyme-Based Electrolytes for Batteries with Sodium or Graphite as Electrode, ACS Appl. Mater. Interfaces. 11 (2019) 32844–32855. https://doi.org/10.1021/acsami.9b06760.

[58] V.A. Agubra, J.W. Fergus, The formation and stability of the solid electrolyte interface on the graphite anode, J. Power Sources. 268 (2014) 153–162. https://doi.org/10.1016/j.jpowsour.2014.06.024.

[59] W. Mei, L. Jiang, C. Liang, J. Sun, Q. Wang, Understanding of Li - plating on graphite electrode : detection , quantification and mechanism revelation, Energy Storage Mater. 41 (2021) 209–221. https://doi.org/10.1016/j.ensm.2021.06.013.

[60] C. Birkenmaier, B. Bitzer, M. Harzheim, A. Hintennach, T. Schleid, Lithium Plating on Graphite Negative Electrodes: Innovative Qualitative and Quantitative Investigation Methods, J. Electrochem. Soc. 162 (2015) A2646–A2650. https://doi.org/10.1149/2.0451514jes.

[61] S. Komaba, T. Hasegawa, M. Dahbi, K. Kubota, Potassium intercalation into graphite to realize high-voltage/high-power potassium-ion batteries and potassium-ion capacitors, Electrochem. Commun. 60 (2015) 172–175. https://doi.org/10.1016/j.elecom.2015.09.002.

[62] J.C. Pramudita, V.K. Peterson, J.A. Kimpton, N. Sharma, Potassium-ion intercalation in graphite within a potassium-ion battery examined using in situ X-ray diffraction, Powder Diffract. 32 (2017) S43–S48. https://doi.org/10.1017/S0885715617000902.

[63] K. Kubota, M. Dahbi, T. Hosaka, S. Kumakura, S. Komaba, Towards K-Ion and Na-Ion Batteries as "Beyond Li-Ion," Chem. Rec. 18 (2018) 459–479. https://doi.org/10.1002/tcr.201700057.

[64] X. Yang, Z. Su, D. Wu, S.L. Hsu, H.D. Stidham, Raman analysis of a conformational distribution of poly(ethylene oxide) and its model compound in the liquid state, Macromolecules. 30 (1997) 3796–3802. https://doi.org/10.1021/ma961804v.

[65] G.D. Smith, R.L. Jaffe, D.Y. Yoon, Conformations of 1,2-Dimethoxyethane in the Gas and Liquid Phases from Molecular Dynamics Simulations, J. Am. Chem. Soc. 117 (1995) 530–531. https://doi.org/10.1021/ja00106a061.

[66] Y. Ogawa, M. Ohta, M. Sakakibara, H. Matsuura, I. Harada, T. Shimanouchi, Vibration Spectra and Rotational Isomerism of Chain Molecules. V. 2,5-Dioxahexane, 2,5-Dithiahexane, and 2-Oxa-5-thiahexane, Bull. Chem. Soc. Jpn. 50 (1977) 650–660. https://doi.org/10.1246/bcsj.50.650.

[67] M. Salama, I. Shterenberg, H. Gizbar, N.N. Eliaz, M. Kosa, K. Keinan-Adamsky, M. Afri, L.J.W. Shimon, H.E. Gottlieb, D.T. Major, Y. Gofer, D. Aurbach, Unique Behavior of Dimethoxyethane (DME)/Mg(N(SO2CF3)2)2 Solutions, J. Phys. Chem. C. 120 (2016) 19586–19594. https://doi.org/10.1021/acs.jpcc.6b07733.

[68] Y. Yamada, M. Yaegashi, T. Abe, A. Yamada, A superconcentrated ether electrolyte for fast-charging Li-ion batteries, Chem. Commun. 49 (2013) 11194–11196. https://doi.org/10.1039/c3cc46665e.

[69] L. Jiang, C. Yan, Y. Yao, W. Cai, J. Huang, Q. Zhang, Inhibiting Solvent Co-Intercalation in a Graphite Anode by a Localized High-Concentration Electrolyte in Fast-Charging Batteries, Angew. Chemie Int. Ed. 60 (2021) 3402–3406. https://doi.org/10.1002/anie.202009738.

[70] J. Wang, Y. Yamada, K. Sodeyama, C.H. Chiang, Y. Tateyama, A. Yamada, Superconcentrated electrolytes for a high-voltage lithium-ion battery, Nat. Commun. 7 (2016) 1–9. https://doi.org/10.1038/ncomms12032.

[71] M. Kerner, N. Plylahan, J. Scheers, P. Johansson, Thermal stability and decomposition of lithium bis(fluorosulfonyl)imide (LiFSI) salts, RSC Adv. 6 (2016) 23327–23334. https://doi.org/10.1039/c5ra25048j.

[72] K. Kimura, J. Motomatsu, Y. Tominaga, Correlation between Solvation Structure and Ion-Conductive Behavior of Concentrated Poly(ethylene carbonate)-Based Electrolytes, J. Phys. Chem. C. 120 (2016) 12385–12391. https://doi.org/10.1021/acs.jpcc.6b03277.

[73] W. Xu, H. Wang, J. Hu, H. Zhang, B. Zhang, F. Kang, D. Zhai, A highly concentrated electrolyte for high-efficiency potassium metal batteries, Chem. Commun. 57 (2021) 1034–1037. https://doi.org/10.1039/D0CC07266D.

[74] I. Escher, Y. Kravets, G.A. Ferrero, M. Goktas, P. Adelhelm, Strategies for Alleviating Electrode Expansion of Graphite Electrodes in Sodium-Ion Batteries Followed by In Situ Electrochemical Dilatometry, (2021). https://doi.org/10.1002/ente.202000880.

[75] N. Leifer, M.F. Greenstein, A. Mor, D. Aurbach, G. Goobes, NMR-Detected Dynamics of Sodium Co-Intercalation with Diglyme Solvent Molecules in Graphite Anodes Linked to Prolonged Cycling, (2018). https://doi.org/10.1021/acs.jpcc.8b06089.

[76] H. Kim, J. Hong, G. Yoon, H. Kim, K.Y. Park, M.S. Park, W.S. Yoon, K. Kang, Sodium intercalation chemistry in graphite, Energy Environ. Sci. 8 (2015) 2963–2969. https://doi.org/10.1039/c5ee02051d.

[77] Q. Liu, F. Wu, D. Mu, B. Wu, A theoretical study on Na+ solvation in carbonate ester and ether solvents for sodium-ion batteries, Phys. Chem. Chem. Phys. 22 (2020) 2164–2175. https://doi.org/10.1039/c9cp05636j.